nature communications



Article

https://doi.org/10.1038/s41467-025-63939-5

Static mechanical cloaking and camouflage from disorder

Received: 25 February 2025

Accepted: 2 September 2025

Published online: 06 October 2025

Check for updates

Zhou Yang^{1,2,8}, Jianlin Yi^{3,4,8}, Fenglei Li^{1,2}, Zheng Li⁵, Lin Ye⁶, Bing Li $\mathbb{O}^{1,7} \boxtimes \&$ Johan Christensen $\mathbb{O}^2 \boxtimes$

Architected materials with advanced functionalities are increasingly employed in fields such as biomedicine and robotics. While periodic designs have been predominant, disordered materials inspired by natural irregularities have recently gained prominence for their potential to high damage tolerance, isotropy, and imperfection insensitivity. However, the advantages of such irregular materials remain debated. Here, inspired by a pioneering stochastic growth rule, we present an irregular growth strategy that uses a limited set of cells to engineer mechanical stealth, achieving both static cloaking and camouflage within a narrow error tolerance—a feat challenging for periodic designs. Our approach demonstrates adaptability to diverse boundary loads and void configurations, ensuring reliable performance without requiring extensive datasets. Arbitrary cloaks generated with minimal samples retain camouflage under varied conditions, including mutual camouflage between targets with disparate void shapes. This framework is further extended to three-dimensional scenarios, highlighting its potential for cloaking and camouflage across multiscale applications.

The meticulous engineering of microarchitecture has led to the development of a diverse range of architected materials with exceptional properties, which have been extensively applied across mechanics¹⁻⁴, electromagnetism⁵⁻⁷, acoustics⁸⁻¹⁰, and robotics^{11,12}. Specifically in mechanics, the extraordinary properties of architected materials, such as ultrastiffness^{13,14}, ultralight^{13,15}, negative stiffness and poisson's ratio¹⁶⁻²⁰, skin effects²¹, programmability²², have been universally presented. These functionalities are primarily derived from their uniquely engineered geometries and topologies rather than chemical compositions. Traditionally, most architeched materials have been designed with periodicity to simplify the design process²³⁻²⁶. However, natural materials—such as bone²⁷, toucan beak, dragonfly wing, water lily²⁸, and wood²⁹—are typically characterized by a lack of periodicity, in contrast often exhibiting superior functionalities.

Inspired by these irregular natural structures, disordered architeceted materials have recently been engineered to offer advanced functions, including high damage tolerance^{30–32}, perfect isotropic³³, and imperfection insensitivity³⁴, etc.

Natural variation in the shape of biomaterials is a result of their self-organizing growth. This growth occurs through a decentralized, probabilistic construction process that adheres to straightforward local guidelines, rather than being directed by a central blueprint³⁵. Consequently, compared to the traditional periodic architectures, irregular architected materials can offer a vastly expanded design space for structural geometry. However, this expanded design space gives rise to increased complexity and strong nolinearity in geometry modeling. To address this challenge, several pioneering methods for designing irregular or disorderd architected materials have been

¹School of Aeronautics, Northwestern Polytechnical University, Xi'an, China. ²IMDEA Materials Institute, Getafe, Madrid, Spain. ³Department of Engineering Mechanics, CNMM and AML, Tsinghua University, Beijing, China. ⁴State Key Laboratory of Nonlinear Mechanics, Institute of Mechanics, Chinese Academy of Sciences, Beijing, China. ⁵State Key Laboratory for Turbulence and Complex Systems, Department of Mechanics and Engineering Science, College of Engineering, Peking University, Beijing, China. ⁶School of System Design and Intelligent Manufacturing (SDIM), Southern University of Science and Technology, Shenzhen, China. ⁷National Key Laboratory of Strength and Structural Integrity, Xi'an, China. ⁸These authors contributed equally: Zhou Yang, Jianlin Yi. e-mail: bingli@nwpu.edu.cn; johan.christensen@imdea.org

proposed, including stochastic bond removal and addition³⁶, node replacement in regular materials³⁷, framework for disorder cellular metamaterials³⁸ and bio-inspired irregular growth techniques³⁴. Liu et al, initially demonstrated that irregular architected materials, designed via random growth based on predefined adjacency rules, possess diverse and superior properties of stress regulation^{34,39}. Liu et al. further developed this random growth approach and expanded the enhancement potential of irregular architected materials in the functionality of sound absorption⁴⁰. Furthermore, a recently developed aperiodic monotile truss lattice and polymer interpenetrating phase composites demonstrate significant improvements in strength and toughness⁴¹. However, up to now, research on irregular architected materials remains in its infancy. Controversies and doubts stills persist regarding their mechanical properties such as damage insensitivity and other diverse functionalities in irregular structures³⁴, warranting further exploration to inspire more exotic and unique characteristics. Therefore, it is worthwhile to further advance the irregular architected materials, ranging from the design framework, growth methodology to function expansion, targeting on achieving more versatile, superior funcationalities not possible with periodic structures.

Meanwhile, as a topic of particular interest, cloaking has attracted ever-increasing attention in multiple physical fields electromagnetics⁴²⁻⁴⁴, optics^{45,46}, thermodynamics^{47,48} and acoustics^{49,50}. Nonetheless, static mechanical cloaking poses unique challenges, as material-parameter transformations, effective in other physics, are inapplicable. In static mechanics, the governing equation can not satisfy the form invariance under transformation, making perfect mechanical cloaking theoretically unattainable⁵¹⁻⁵³. Additionally, the use of 4-rank tensors to describe the mechanical response adds complexity to the design of the cloak. Thus, only approximate mechanical cloaking effects can be realized within a narrow tolerance. Exisiting mechanical cloak designs typically rely on direct lattice transformation^{52,54}, periodically bimode or pentamode materials^{55,56}, or topological optimazation^{57,58}. While these methods have shown prospect, they are often limited by computational complexity or an inability to handle complex geometric voids. In terms of rich structural responses of irregular architected materials, the distinctive mechanical behaviors offer innovative prospects for the engineering of mechanical cloaks. Additionally, camouflage, which can be applied for stealth technology⁵⁹, thermal management⁶⁰, and multispectral concealment⁶¹, has been extensively explored in electromagnetic manipulations and thermodynamics, but absent in the control of static mechanical deformation. Therefore, introducing irregular structures into mechanical cloaking and camouflage design presents an intriguing research avenue.

Here, we propose an irregular growth strategy based on a varying stiffness rule to generate irregular architected materials, experimentally demonstrating that outstanding static mechancial cloaking and camouflage can emerge directly from the disorder inherent in these structures. The so-called mechanical cloaking device can make a void structure perform as if it is defect-free, thereby achieving protective functionality. Beyond that, the camouflage cloak enables a void structure to mimic the mechanical response of another, offering diverse functional potentials. It holds promise in VR⁶² and gaming for creating haptic illusions, in soft robotics for concealing mechanical signatures, and in biomedical devices for replicating tissue-like tactile feedback. Moreover, it supports the design of mechanical metamaterials with adaptive or programmable behaviors under varied loading conditions. Notably, the proposed method requires only a small number of unit cells with simple configurations, greatly simplifying manufacturing and implementation compared to approaches that rely on large unit cell libraries, topology optimization and manual adjustment. In addition to achieving static mechanical cloaking, the framework enables static mechanical camouflage under complex void shapes and boundary conditions, including mutual camouflage between different voids. Furthermore, the same structure robustly

suppresses void-induced distortions and maintains effective camouflage across varying loading conditions. Even in non-uniform surroundings, it significantly mitigates the global deformation of the structure.

Irregular growth strategy

As illustrated in Fig. 1, we present a design strategy for generating irregular structures capable of static mechanical cloaking and camouflage for arbitrarily shaped voids. A butterfly-shaped void is selected as an example, where the cloak region (Ω_c) surrounds the void and the background region ($\Omega_{\rm s}$) consists of periodically arranged microstructures. Several types of basic building blocks with varying stiffness are meticulously designed to fill the cloak region based on the proposed growth rules. Through interative virtual growth process, numerous irregular structures can be created, with the resulting cloak maintaining the static response of the background material under complex loads as if no void or another entirely different void were present. Additionally, the cloak can mimic the responses of other void shapes, such as an elephant or a star, demonstrating excellent mutual camouflage effects. Our irregular growth method for static mechanical cloaking and camouflage holds promising applications across scales, from micro- to macroscale, including multifunctional cloaks for chips, bio-skeletal scaffolds and tunnel support structures.

We first detail our growth method for generating irregular structures, as illustrated in Fig. 2. This growth framework consists of four key components: the basic constitutive building blocks, the adjacency rules governing block connections, the proportional distribution of each block class, and the underlying grid of target structure to be filled. Unlike the existing virtual growth procedure³⁴, we ensure connectivity and minimize defects by constructing the building blocks with symmetric geometries, enabling seamless connections between any two blocks. For manufacturing ease and design simplicity, a series of basic microstructural building blocks with increasing stiffness and uniform dimensions are designed through a step-by-step material removal approach, starting from solid unit cells and combined with simulation analysis (as described in Fig. 2a, and Methods section). These blocks can be categorized into four classes according to their stiffness level. The fourth class consists of a single solid block without any microstructure, exhibiting the highest stiffness. Here, the four classes are defined as four sets, Class I: $S_1 = \{B_1, B_2, B_3\}$, Class II: $S_2 = \{B_4, B_5, B_6\}$, Class III: $S_3 = \{B_7, B_8, B_9\}$ and Class IV: $S_4 = \{B_{10}\}$. B_i is the block code, showing in Fig. 2a. For the irregular growth, the normalized probability of an admissible block $\Gamma(B_i)$ is formulated as

$$\Gamma(B_i) = \frac{n_i}{\sum_{j=1}^m n_j}, i \in [1, m]$$
(1)

where n_i is the number of occurrences of block B_i within the database, and m represents the number of block types (here, m=10). The expression $\sum_{j=1}^{m} n_j$ denotes the total number of occurrences for all blocks B_1 , B_2 , ..., B_m within the database. The database comprises a limited number of reusable building blocks. Subsequently, the initial proportion of the jth class sets, ξ_i^0 , can be calculated as

$$\xi_j^0 = \sum_{B_i \in S_j} \Gamma(B_i), j \in [1, 4]$$
 (2)

By default, the initial proportion of each block $\Gamma(B_i)$ is set to a given constant (e.g., $\Gamma(B_i)$ =10%), then the initial proportion of each class in database can be calculated as ξ_1^0 =30%, ξ_2^0 =30%, ξ_3^0 =30%, ξ_4^0 =10%, respectively. When one of the initial proportions ξ_j^0 changes, the proportion of the rest types of blocks are set to be equal, ensuring that $\sum_{j=1}^4 \xi_j^0$ =1.

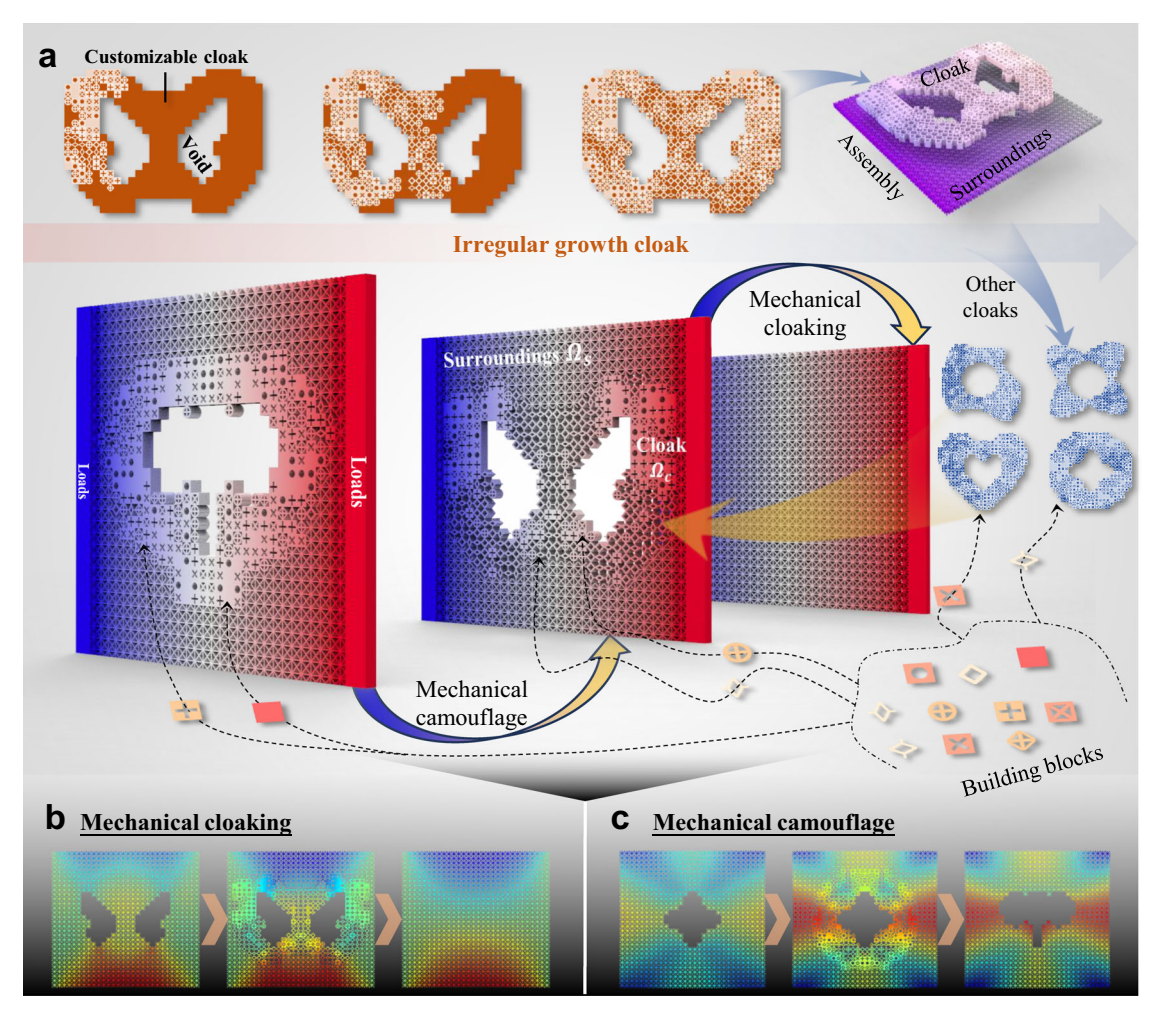


Fig. 1 | **Schematic diagram of disorder mechanical cloak design strategy incorporating irregular growth. a** The irregular growth process of a cloak with butterfly-shaped void is presented. The definition of void, cloak, and surroundings region in an entire structure is demonstrated, and for different voids, the cloaks can vary. With the help of cloak irregularly built by ten blocks, structure with voids can

possess displacement field distribution almost same to its reference structure which is reflected in the uniform gradient color. Finally, mechanical cloaking and camouflage effect can be achieved. **b**, **c** Examples of mechanical cloaking and camouflage.

The adjacency rules are defined as follows. In k^{th} step, the randomly selected block $B_i^k \in S_j$ will be filled into a position $P_{(x_k,y_k)} \in \Omega_c$, as shown in Fig. 2b. As a result, the availability of different types of blocks in adjacent positions $P_{(x_k+1,y_k)}$, $P_{(x_k,y_k+1)}$, $P_{(x_k-1,y_k)}$ and $P_{(x_k,y_k-1)}$ are influenced. For any position $P_{(x,y)} \notin \Omega_c$, such as $P_{(x_k-1,y_k)}$ and $P_{(x_k,y_k-1)}$ showing in Fig. 2b, they will not contribute to the next choice. After the selection of B_i^k , the current permissible block B_p^k in adjacent positions have to meet the requirement $B_p^k \in S_{j-1} \cup S_j \cup S_{j+1}$ ($S_0 = S_5 = \emptyset$), as illustrated in Fig. 2c. Simultaneously, these adjacent positions may have already influenced by previous operations. Assume that, in $(k-1)^{\text{th}}$ step, the alternative blocks' set in any influenced position $P_{(x,y)}$ is $S_{(x,y)}^{k-1}$. Consequently, in the current adjacent positions, the final alternative blocks' set $S_{(x,y)}^k = S_{(x,y)}^{k-1} \cap (S_{j-1} \cup S_j \cup S_{j+1})$. As a result, the alternative class proportion S_j^k in adjacent positions for S_j^k step should be updated as

$$\xi_{j}^{k} = \frac{\sum_{B_{i} \in S_{j}} \sum_{i \in S_{i(x,y)}} \Gamma(B_{i})}{\sum_{B_{i} \in S_{i(x,y)}} \Gamma(B_{i})}, j \in [1, 4], k \in [1, n_{g}]$$
(3)

where n_{σ} is the number of grids within cloak region.

To determine the next position to be filled, we introduce a factor e, presented in each grid (Fig. 2d), as $e = \log_{N_s} n_p$, in which n_p is the total number of permissible types of blocks in specific position and N_s is the

total number of different types of blocks. Notably, at initial state, the e value in each grid is the same, with e=1, as n_p equals N_s . After the first choice, the subsequent choice B_i^{k+1} , selected from the database, should fill into the position with the minimum factor value e_{\min} . During each growth step, the block that satisfies the adjacency rules is randomly selected from the database with equal probability, where the block proportion in database is not deliberately changed. Therefore, a stochastic generation of irregular structures can be readily constructed by following this irregular growth rule when the underlying grid of a target structure is given, regardless of the target shape.

To illustrate, a part of permissible cloak region, meshed as a 5×5 chessboard, is extracted as an example to illustrate the growth process, as described in Fig. 2d. In the initial step, we must specify an initial growth position, which can be the corner or any other position throughout the chessboard. Then, a building block is randomly selected from database to fill in the initial position $P_{(x_1,y_1)}$. As a result, the adjacent positions' permissible choice of blocks is changed according to the adjacent, leading to a smaller e value. Subsequently, the adjacent position with e_{\min} is selected, or, in cases of ties, a position will be randomly chosen from the grids with same e_{\min} value and filled with a randomly selected block from the permissible set S_j . After each selection, the e values of the positions adjacent to the filled locations are updated according to the adjacency rules to determine the next position to be filled. And this growth process is repeated until all

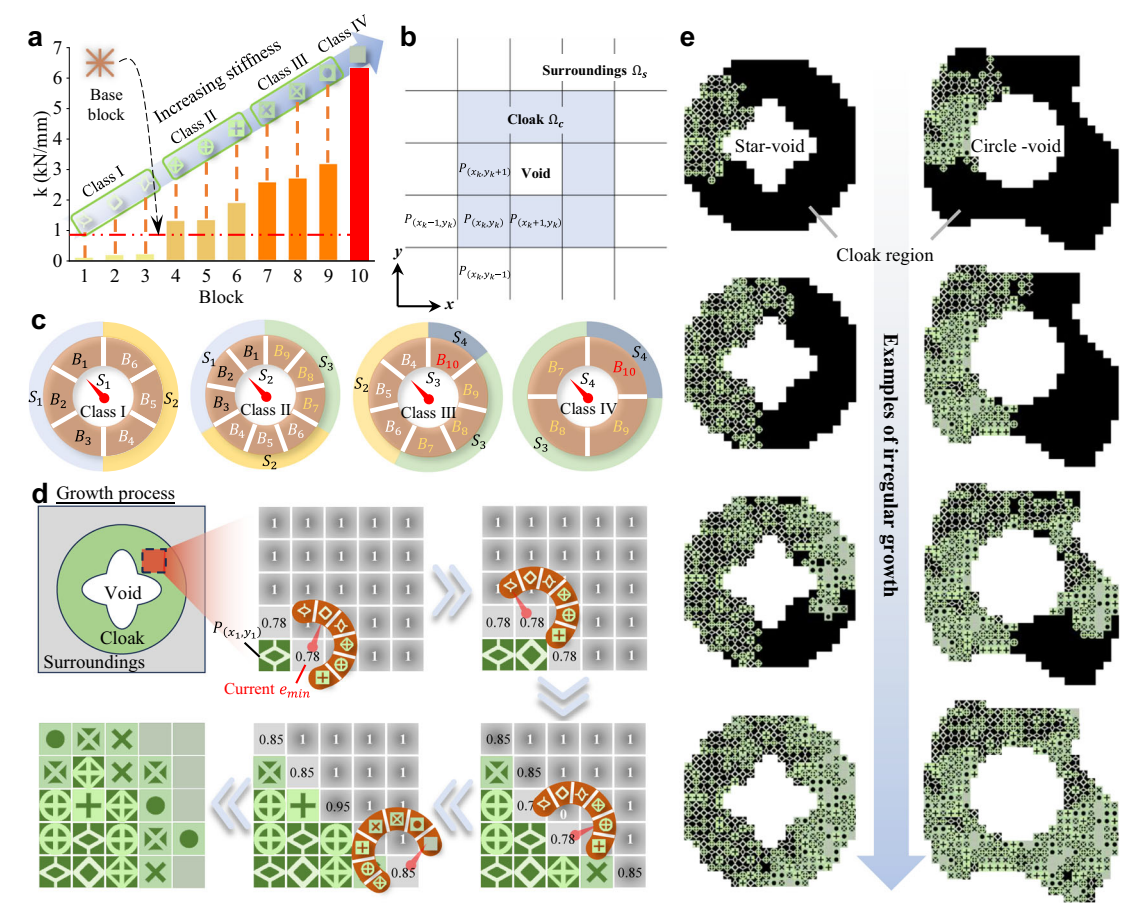


Fig. 2 | **Stiffness gradient-based irregular growth structural design strategy. a** The stiffness of block is obtained through uniaxial compression testing and the buildings blocks are divided into four classes according to their stiffness level. The base block's stiffness level is marked as dashed line to highlight the stiffness differences of various class of blocks relative to their surrounding environment. **b** Sketch map for demonstrating how the chosen block in a position affects its

adjacent positions while choosing the next block to fill in. **c** The adjacency rule of blocks in each class is illustrated and the code B_i in the rings are the indexes of blocks shown in (**a**), S_i is a set containing several types of blocks. **d** The detailed growth process of generating a 5×5 square based irregular structure which is extracted from the permissible cloak region. **e** Demonstration of the process for generating irregular structures based on circular and irregular underlying grid.

positions are filled, ultimately achieving a stochastically irregular structure. This approach can be applied to generate an arbitrary-shaped, irregular cloak Ω_c for a corresponding given grid, as demonstrated in Fig. 2e and Supplementary Movie 1. It is clearly presented that for any void structure, regardless of its complicated void geometries and size, the proposed framework enables rapid and customized growth of irregular structures once the growth region is given. More details regarding the entire design framework are presented in Supplementary Note 1.

Results

Cloaking and camouflage under complex boundary conditions

In this section, we evaluate the effectiveness of our irregular growth strategy in achieving the challenging functionalities of static mechanical cloaking and camouflage. We begin with the cloaking effect for a circular void. As illustrated in Fig. 3a, a reference structure, without a cloak or void, consists of 30 × 30 identical blocks arranged in a periodic pattern. Each base square block measures 5 mm in width and contains four crossed bars, each 0.5 mm wide (see inset). The void structure is identical to the reference structure but includes a central circular void with a radius of 30 mm. The cloak structure includes a circular cloak with a 55 mm radius surrounding the void, approximately 1.83 times the void size, while the background blocks outside the cloak are identical to those in the reference structure. The cloak structure is generated by applying the proposed irregular growth to a quarter of the circular cloak, followed by symmetric replication.

A tensile displacement load is applied to the upper and lower boundaries of the structures, (d_y = 0.75 mm along the y direction, d_x = 0 mm along the x direction), as shown in the inset of Fig. 3a. The structures experience approximately 1% strain within the linear elastic regime. Numerically simulated overall displacement field of the void and reference structures under the same loading conditions are compared in Fig. 3a. Significant differences between the intact and void displacement responses are captured. In the reference structure, displacement changes approximately uniformly from the center to the upper/lower boundaries, while in the void structure, displacement filed is significantly distorted due to the void.

To quantitatively characterize the difference between the displacement response of the void/cloak structures and the reference structure under the same loading conditions, we measure the relative displacement differences in the surrounding region Ω_s . Three difference indexes, the x-direction displacement difference Δ_u , the y-direction displacement difference Δ_v , and the total displacement difference Δ , are defined and calculated as

$$\Delta_{u} = \frac{\sqrt{\sum_{\Omega_{s}} (u_{i} - u_{0,i})^{2}}}{\sqrt{\sum_{\Omega_{s}} (u_{0,i})^{2}}}, \Delta_{v} = \frac{\sqrt{\sum_{\Omega_{s}} (v_{i} - v_{0,i})^{2}}}{\sqrt{\sum_{\Omega_{s}} (v_{0,i})^{2}}}, \Delta = \frac{\sqrt{\sum_{\Omega_{s}} |d_{i} - d_{0,i}|^{2}}}{\sqrt{\sum_{\Omega_{s}} |d_{0,i}|^{2}}}$$
(4)

where $u_i(u_{0,i})$ and $v_i(v_{0,i})$ are the nodal displacements of the void/cloak (reference) structure along the x and y directions, respectively,

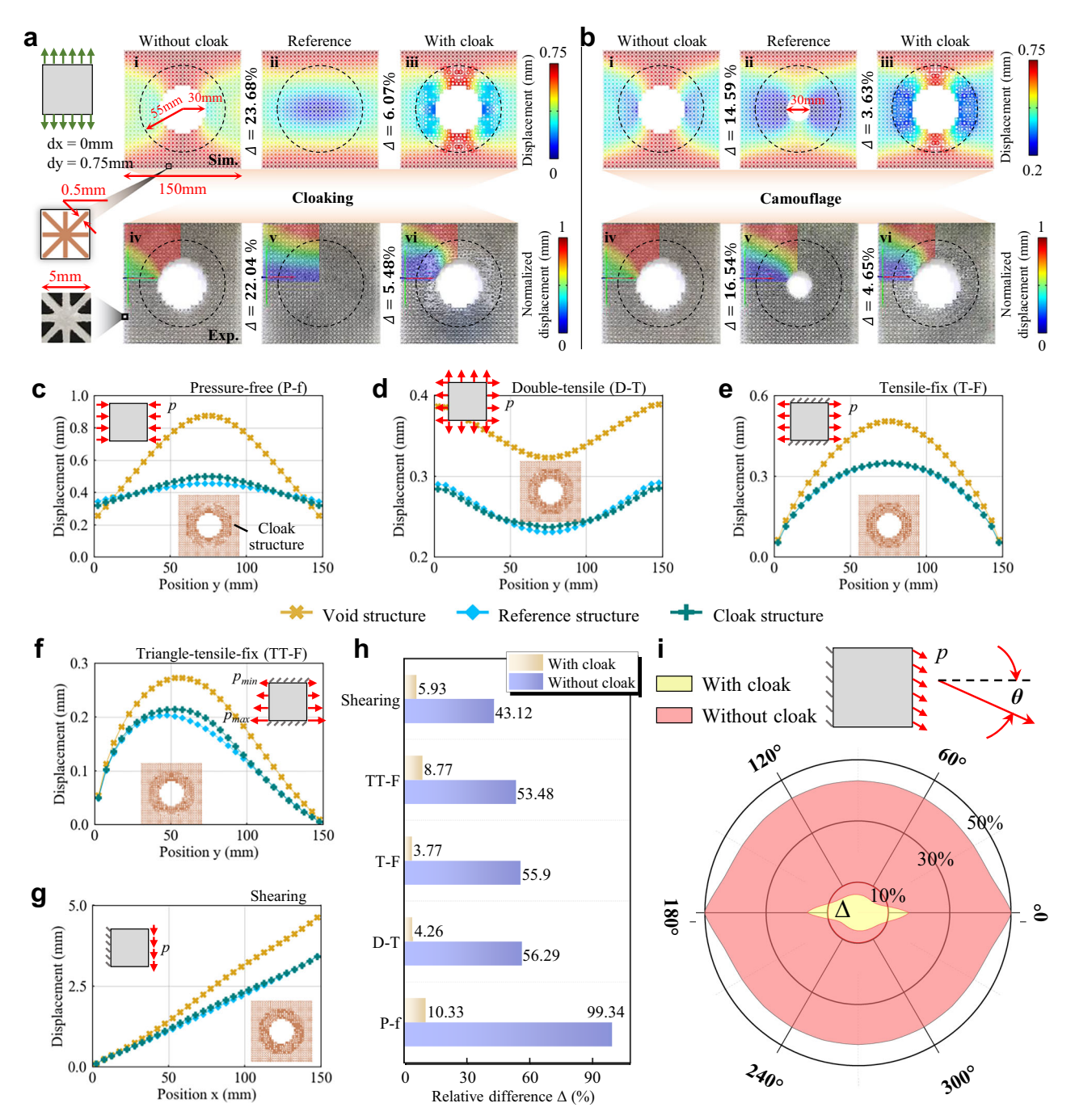


Fig. 3 | The resultant mechanical cloaking performance under tensile loading and camouflage performance under different loadings. a The simulated displacement field of void structure, reference structure, and cloak structure for cloaking (a-i to iii) and their corresponding experiment results (a-iv to vi). b The simulated displacement field of void structure, reference structure and cloak structure for camouflage (b-i to iii) and their corresponding experiment results

(**b**-iv to vi). **c**-**f** Displacement curves of void, reference and cloak structures' left boundary under P-f, D-T, T-F and TT-F loadings. **g** Displacement curves of structural upper boundary under shearing loads. **h** The relative differences of cloak and reference structures under different loads. **i** The radar chart of the overall relative difference under different loading angles.

and $d_i = (u_i, v_i)$ and $d_{0,i} = (u_{0,i}, v_{0,i})$ represent the corresponding nodal displacement vector of the void/cloak and reference structures, respectively. Lower values of Δ_u , Δ_v , especially Δ , indicate a better cloaking or camouflage performance.

For the basic case of a circular void, the relative displacement difference of the void structure is calculated as $\Delta = 23.68\%$. A series of irregular cloak structures are generated by using the proposed irregular growth strategy. In this work, we set the total number of the irregular structures of irregular growth for each case is N = 1000, which is a very small sample quantity compared with tens of thousands

of quantities. The relative displacement differences of the 1000 virtual cloak structures are shown in Supplementary Fig. 2a. It is observed that a considerable amount of irregular cloak structures generated by using the proposed framework exhibit relative displacement differences of less than 10%. Notably, the static displacement response of the cloak structure with the minimum $\Delta\!=\!6.07\%$ is presented in Fig. 3a-iii, demonstrating superb cloaking performance. The deformation field in the surrounding region Ω_{s} of this cloak structure is almost same as that of the reference structure. The specimens using nylon fiber-reinforced materials via Selective Laser Sintering (SLS) 3D printing technology,

exhibiting a structurally coherent and aesthetically refined surface, characterized by its uniformity and smoothness. The simulation results are verified by tensile testing and Digital Image Correlation (DIC) technology. For more details, see Methods. The experiment results are shown in Fig. 3a-iv to vi, in which the Δ value of the void structure is 22.04% and that of the cloak structure is significantly reduced to 5.48%, aligning well with the numerical results and further confirming the excellent cloaking effect of the irregular-growth structures. Remarkably, besides the advantages of few samples and efficient applicability for arbitrary-shape voids, the generated irregular cloak exhibits small size region, yet still shows impressive cloaking performance. This suggests that our method allows for achieving static mechanical cloaking within a smaller cloak region⁵³ and a specific tolerance range by modifying the underlying grid.

We further demonstrate that our irregular growth method can be used to design mechanical camouflage device. Firstly, we begin with a simple reference structure with a small center void (radius 15 mm), as shown in Fig. 3b. We verify the mechanical camouflage functionality by performing that the irregular cloak structure with a larger void can achieve the same static responses as the reference structure. Specifically, without the cloak, the displacement response of the structure with a larger void has a significant difference, Δ =14.59%, from that of the reference structure, as shown in Fig. 3b-i and ii. Using our irregular growth method, the response difference of a cloak structure can realize a significant four-time decrease to Δ =3.63% within a small sampling database of 1000 virtual cloak structures. The database values of Δ_u , Δ_v , and Δ are shown in Supplementary Fig. 2b. The displacement field of the cloak structure with the larger circular void closely matches that of the reference structure with the small void, demonstrating exceptional camouflage performance. The experimental results have also effectively corroborated this point, where the experimentally measured Δ reduces from 16.54% (the large void structure) to 4.56% (the cloak structure), as shown in Fig. 3b-iv to vi.

As additional evidence of the applicability of our method in mechanical camouflage design, we evaluate the camouflage performance under five additional complex loading conditions: Pressurefree (P-f), Double-tensile (D-T), Tensile-fix (T-F), Triangle tensile-fix (TT-F), and shearing, as illustrated in the insets of Fig. 3c-g. The magnitudes of these loads are given as p=88 MPa, $p_{min}=0 \text{ MPa}$, $p_{\text{max}} = p$. Figure 3c-f display the displacement amplitude responses at the left boundary of the void, reference and cloak structures for the loading conditions of P-f, D-T, T-F, and TT-F. For the shear case, we observe the amplitude response at the upper structure boundary, see Fig. 3g. It is observed that the response curves of the cloak structures closely match those of the reference structure under all loading conditions mentioned above, but significantly differ from those of the void structure. As compared in Fig. 3h, the optimal cloak structure for each case shows a significant reduction in Δ by 89.6%, 92.43%, 93.26%, 83.6%, and 86.25%, respectively (Fig. 3h, Δ_{u} and Δ_{u} in Supplementary Fig. 2). Compared to the corresponding void structures without a cloak, it verifies the extraordinary camouflage performance under all complex boundary conditions. The structural details of the optimal cloak for each boundary load are presented in the inset of Fig. 3c-g, and their displacement fields are supplemented in Supplementary Fig. 3.

Demonstrating the robustness of a single cloak under varying loading conditions, we select the camouflage design under shearing loads as an example. As shown in Fig. 3i, fixing the left boundary and applying a load p (with a loading angle varying from 0° to 360°) at the right boundary, we find that, except near the extreme 0° and 180° loading angles, the Δ of a same cloak structure is always below 10%, indicating remarkable robustness of our irregular cloak method for camouflage performance. The displacement field diagrams at various loading angles are presented in Supplementary Movie 2.

Camouflage for complex geometries

For voids with more complex geometric topologies, such as heartshaped, elephant-shaped, and butterfly-shaped void etc. (see Fig. 4a), the applicability and robustness of our proposed method in mechanical camouflage is further verified. Targeting a reference structure with a small central circular void under P-f loading condition (Fig. 4a), a series of irregular cloak structures for various shapes of voids are built based on the proposed irregular growth strategy. The Δ_u , Δ_v and Δ distributions of cloak structures for each void shape are provided in Supplementary Fig. 4. And the detailed configurations of the final cloak structures for each void shape are illustrated in Fig. 4b, and the relevant displacement fields are supplemented in Supplementary Fig. 5. Besides, the Δ of the void and cloak structures are compared in Fig. 4c. Compared to the void structures without cloak, the Δ of cloak structures has a great decrease of 85.3%, 90.68%, 87.21%, 88.36%, 80.07%, and 79.63% for various void shapes, respectively. The results unambiguously demonstrate the remarkable camouflage effect of the irregular aperiodic cloaks for various complex voids. However, as the complexity of the void shape increases, the camouflage effect deteriorates, as observed in the cases of the elephant and butterfly voids. To mitigate this, an optimization strategy is introduced (see details in Supplementary Note 4), which further reduces the Δ values of these two complex void structures from 28.39 to 14.15% and from 20.97 to 12.14%, respectively, following the initial Δ values of 142.28% and 102.94%, respectively. The cloaking performance has a significant twofold enhancement.

To assess the robustness of camouflage effect, we also calculate the displacement responses for the reference, void, and cloak structures under varying pressure amplitudes. The maximum displacements at the left and upper edges of these structures are captured and compared to characterize the camouflage performance. Two typical voids of ellipse-shape and star-shape are selected as examples, as shown in Fig. 4d, e, the profiles for other shapes are provided in Supplementary Fig. 8. The results show that as the pressure increases, the maximum displacements at the left or upper boundary of the cloak structures remain nearly identical to those of the reference structures, but diverging significantly from those of the void structures. This finding highlights the robust camouflage performance of irregular-growth cloaks.

More intriguingly, the proposed growth method enables mutual camouflage between different complex void structures, as shown in Fig. 4f and Supplementary Fig. 9. For example, under P-f loading, the relative displacement difference Δ between the star-void and the elephant-void structure is 37.46%. If taking the star-void structure as the reference structure, the value of Δ is significantly reduced to 7.88% by applying an irregular cloak to the elephant-void structure. Correspondingly, if taking elephant-void structure as the reference, Δ also has a significant decrease to 8.80% by applying an irregular cloak to the star-void structure for disguising as an elephant-shape. These results further confirm the adaptability and generalizability of our irregular growth method for cloaking and camouflage.

Research on block proportion and sample quantity

To explore the effect of block proportion on cloaking performance using a complex butterfly-shaped void, a displacement load of 0.75 mm is applied to the left and right boundaries, corresponding to a 1% strain. By varying the proportion of each block class from 5 to 95% (in interval of 10%), while keeping the other three classes equal, we generate 300 irregular cloak structures for each proportion case. Thus, resulting in 3000 structures per class, and a total of 12,000 structures. The values of Δ_u , Δ_v and Δ are shown in Fig. 5a. The reference structure without any void and the butterfly-shaped void structure are shown in Fig. 5b. Numerous structures demonstrate excellent cloaking performance, with a representative example (not the best) also shown in Fig. 5b. Compared to the void structure without a cloak, the values of

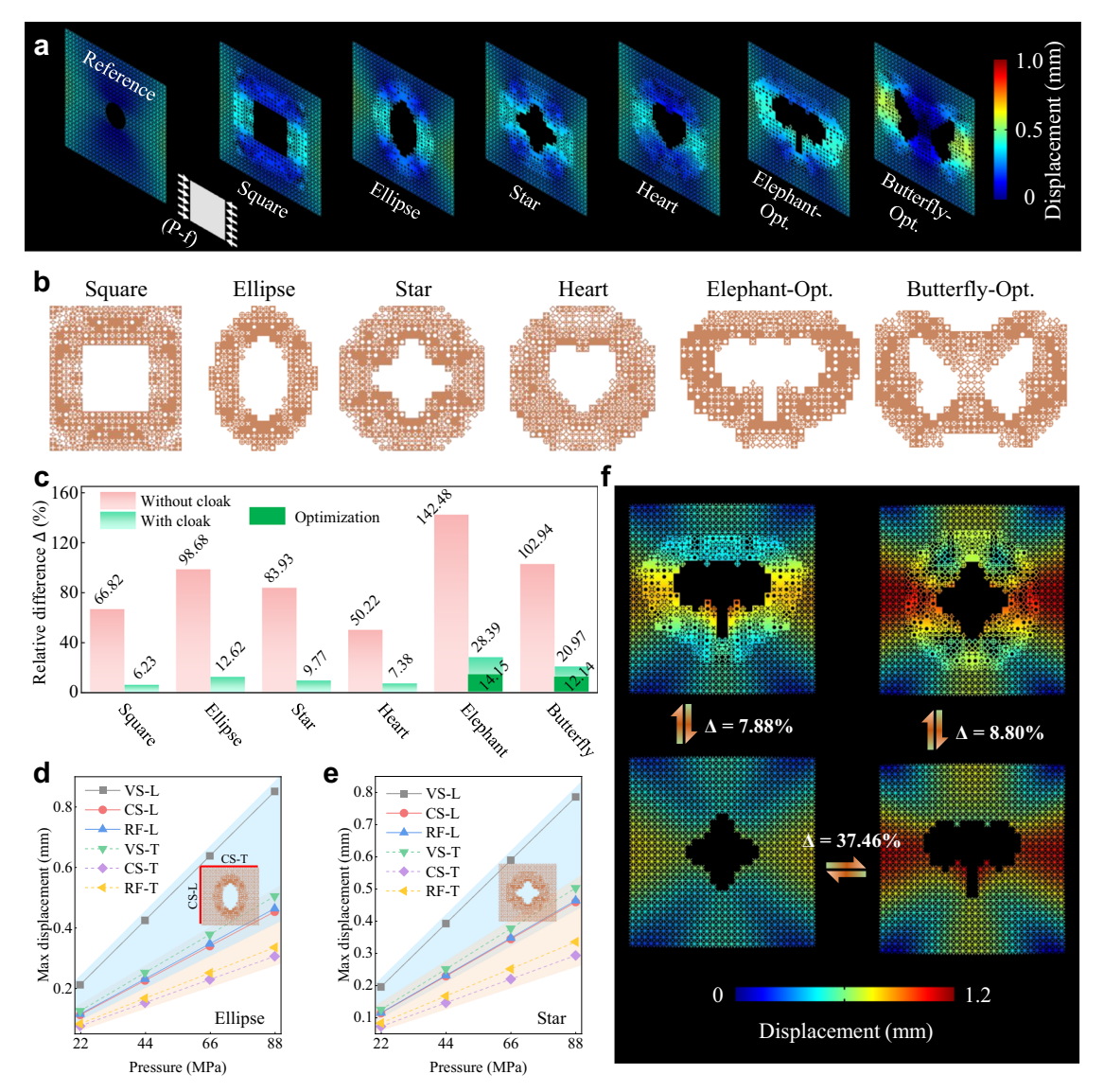


Fig. 4 | Mechanical camouflage performance of cloak structures with different voids under the P-f loading. a Deformation of cloak structures with different voids. The performance of cloak structures with elephant-void and butterfly-void are optimized using optimization algorithm. b Details of cloaks embedded within the cloak structure in A. c Bar chart for the total relative difference Δ of cloak

structures and their corresponding void structures, also the optimization results are presented. **d**, **e** The trend of maximum displacement values of left and upper boundary of each structure as load increase. **f** Mutual camouflage between starvoid structure and elephant-void structure.

 Δ , Δ_u , and Δ_v in the cloak structure decrease from 21.80 to 6.74%, 16.58 to 5.16%, and 46.14 to 12.25%, respectively. And experimental results further validate this cloaking effect (Fig. 5c), showing a reduction in Δ from 25.15% (void structure) to 9.16% (cloak structure).

The probabilities of obtaining favorable outcomes varies with different class proportions. Assuming a 50% reduction in Δ as favorable, Fig. 5d–g show the probability trends for achieving a favorable cloak structure as the proportion of each class increases. This analysis shows that balancing the block proportion is critical for modulating cloaking performance. For the blocks of Class I, it is observed from Fig. 5d that excessively low or high proportions are detrimental. An optimal proportion between 30 and 70% is preferred, as proportions outside this range are less conducive to achieving effective cloaking due to insufficient or excessive stiffness. For Class II, a low proportion is preferable. As illustrated in Fig. 5e, a higher proportion of Class II blocks reduces the likelihood of producing a good cloak structure. Thus, it is advisable to limit the proportion of Class II at 40%, ensuring a more rational composition. Similarly, an excessive proportion of Class III blocks contributes little

to the formation of an effective cloak structure, as illustrated in Fig. 5f. However, a modest proportion of Class III, between 15 and 35%, shows a relatively high occurrence rate of favorable outcomes. Additionally, Fig. 5g shows that a high proportion of solid block (Class IV) significantly lowers the probability of obtaining a good cloak structure. Consequently, the proportion of Class IV block should be restricted to a maximum of 40%. The occurrence rate for favorable cloak structures declines sharply when the proportion of Class II, III or IV exceeds 50%, which should be balanced.

Furthermore, the analysis shows, regardless of the proportion of first three classes, achieving a 50% reduction in Δ_u is consistently feasible, indicating all three classes are vital for mitigating distortion in the loading direction. The occurrence rate for cloak structures achieving a 50% reduction in Δ_u is nearly 100% (Fig. 5d–f). However, the occurrence rate drops dramatically once the proportion of Class IV exceeds 50%, suggesting that producing a cloak structure with effective cloaking capabilities is challenging under such conditions. In summary, a well-calibrated ratio of block classes is conducive to fostering superb cloak structures and optimizing their functionality.

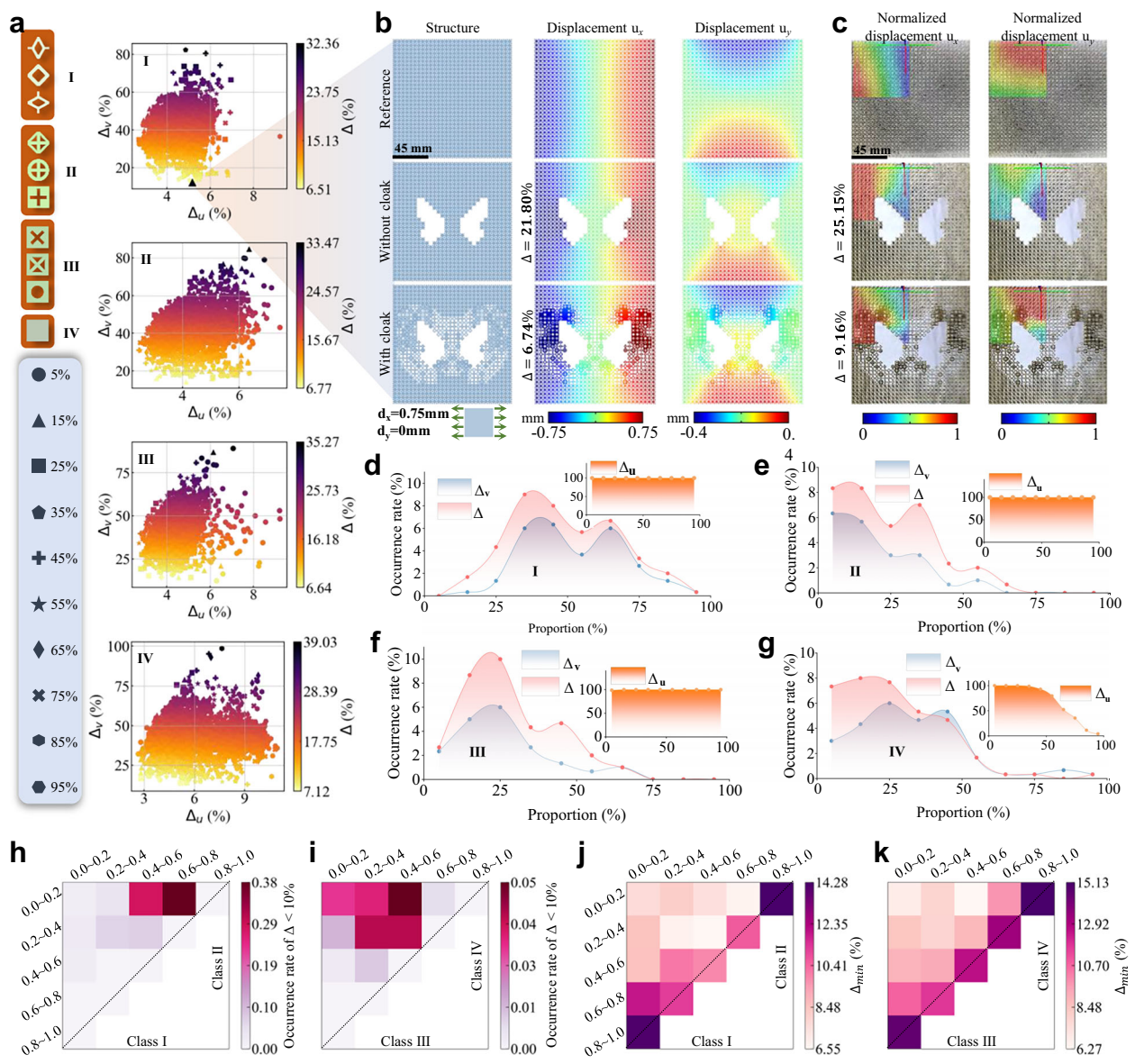


Fig. 5 | The influence of a specific class's proportion on the likelihood of obtaining favorable cloaks. a Scatter plots of the cloak structures' \triangle_u , \triangle_v and \triangle produced by controlling the proportion of each class. **b** The reference, butterfly-void, cloak structures, and their distribution of displacement fields in the x and y directions. **c** The experimental results of the three structures. **d**–**g** show that, in the 3000 samples produced by performing proposed method, the occurrence rate of

producing a cloak structure achieving a reduction of 50% on \triangle , \triangle _u, and \triangle _v changes as the proportion of specific class gradually rise. Occurrence rates of \triangle < 10% with varying block proportions of (**h**) Class I–II and (**i**) Class III–IV, each grid contains 300 samples. \triangle _{min} distributions for every 300 samples under different block proportions of (**j**) Class I–II and (**k**) Class III–IV.

To further investigate the impact of stiffness classes weighting on cloaking performance, we adjust class proportions by varying Class I-II while keeping Class III-IV equal, and by varying Class III-IV while keeping Class I-II equal. When only Class I-II or Class III-IV is present-meaning the structure consists entirely of low-stiffness or high-stiffness unit cells, as shown by the diagonal elements in Fig. 5h, i—it is highly unfavorable for producing cloak structures with Δ < 10%. In contrast, when all the four classes (Class I–IV) are present with balanced proportions, cloak structures with Δ < 10% are more likely to occur. For example, when the proportions of Class I to IV fluctuate around 70%, 10%, 10%, and 10%, respectively, with a variation range not exceeding 10%, 38% of the structures exhibit Δ < 10%, which is highly favorable for achieving excellent cloaking performance. Furthermore, the maximum occurrence rate in Fig. 5h reaches only 5%, substantially lower than the 38% observed in Fig. 5i, highlighting the critical regulatory role played by low-stiffness unit cells. Similarly, when controlling Class I–II and Class III–IV separately, the corresponding Δ_{min} values are shown in Fig. 5j, k. The best-performing structure achieves a Δ_{min} of 6.27%, which also does not appear along the diagonal, but rather in regions where the proportions of all the four classes are balanced. More details are provided in Supplementary Note 7.

Additionally, to reveal the influence of sample quantity on obtaining good results ($\Delta\!<\!10\%$), we take the camouflage of a square hole as a small circular hole as an example to analysis. Under P-f boundary conditions, increasing sample numbers enhance camouflage performance, with Δ reaching 5.2% at 1500 samples (Supplementary Fig. 13a). Besides, we confirm the validity of the proposed method by generating two groups of samples under the same conditions, each consisting of 1000 samples. The two groups show Δ values of 6.23% and 4.25%, respectively, with similar proportions of good results, indicating robust performance (Supplementary Fig. 13b).

Discussion

In this work, we present an irregular growth method based on a limited set of building blocks with varying stiffness, enabling the design of irregular cloaks that achieve excellent mechanical cloaking and camouflage within a narrow tolerance. This method, requiring only a small sampling database, is versatile and applicable to arbitrary-shape voids and complex boundary conditions, allowing the same cloak structure to maintain effective camouflage performance across various loading directions. By altering the underlying network, a wide range of cloaks for complex voids can be generated, demonstrating remarkable camouflage effects. More notably, it allows mutual camouflage between two distinct complex voids. By controlling the block proportions, we elucidate the influence of block proportions on the probability of producing cloaks with desirable performance, and offer corresponding design recommendations. The consistency between simulation and experimental results has been unambiguously validated using 3D printed physical models.

Notably, due to the inherent limitations of 3D printing—such as fabrication accuracy, residual thermal stress, and layer-by-layer deposition induced non-ideal isotropy^{63,64}—printed structures in practice inevitably exhibit a certain degree of anisotropy, which can adversely affect their mechanical performance and hinder large-scale applications. Thereby, we further investigate the effect of material anisotropy on the cloaking and camouflage performance, as detailed in Supplementary Note 9. It is indicated that the proposed method can still realize a nice cloaking and camouflage performance although in consideration of the anisotropic effect, which verifies its robustness and holds its potential for large-scale implementation.

For a step further, the proposed method can generate a variety of irregular structures, resulting in distinct properties for each irregular structure, such as the "cloaked" displacement field discussed in this work. Thereby, introducing irregular topologies into periodic frameworks can greatly expand the mechanical performance, such as Poisson's ratio, Young's modulus, etc. Besides, adjacency rules also play a vital role in the performance of irregular growth algorithm, which is thoroughly discussed in Supplementary Note 10. Determining appropriate adjacency rules can significantly enhance the performance and diversity of static cloaking, as demonstrated by the adjacency rules employed in this work. Additionally, the introduction of blocks with different overall sizes to construct cloak structures is conducive to further enhancing the mechanical performance and helps to reduce the distortion of the displacement field caused by void. For detailed information, see Supplementary Note 11. We further investigate the cloaking performance under more complex loading scenarios, including nonuniform loading, dynamic mechanical cloaking of vibration, and the impact responses (see Supplementary Note 12). Specifically, we conducted both experimental and numerical verifications of static cloaking under a non-uniform complex load, where a favorable cloaking performance is still maintained. Additionally, we successfully achieve cloaking for elastic waves, enabling the void structure, under the effect of the cloak, to exhibit transmission and reflection coefficients identical to those of the defect-free reference structure, along with nearly identical phase and displacement field distributions.

Furthermore, embedding a cloak into an irregular surrounding can substantially reduce the void-induced distortion in displacement field, as shown in Fig. 6a. The overall difference Δ , has a significant reduction, dropping from 482.10% in the void structure to 75.45% with the implementation of the irregular cloak. This method can be further extended to a three-dimensional space, for instance, in a 3D homogeneous medium, cloak or protective structures can be generated through irregular attachment growth (see Fig. 6b). Additionally, for the continuous protection requirements of different cross-sections, such as tunnel construction, the cloak structure with each layer possessing

different void and cloak configurations can also be generated, see Supplementary Note 13. By modifying the block geometries, the adjacency rules, and even the underlying grid, this method can be leveraged to explore a wide range of intriguing non-periodic 3D structures.

Incorporating machine learning and optimization algorithms, this approach can be further refined to customize non-periodic structures with specific functionalities. For example, in chip technology, an increase in temperature can lead to uneven thermal expansion, causing the failure in load-bearing circuit components, short circuits or leakage currents (Fig. 6c). Hence, exploring a micro-scale thermomechanical coupling cloak to achieve uniform heat dissipation and deformation control is highly meaningful. Additionally, for medical care, drilling and nailing bones is a common therapeutic approach to help patients recover from fractures, bone tumors, skeletal deformities, and other conditions. This method could be applied to support damaged bones, helping maintain structural integrity and basic functionality (Fig. 6d). To demonstrate, the irregular cloak is introduced to a bone-like homogeneous structure to mitigate the void-induced distortion, as shown in Supplementary Fig. 21, which eventually leads a Δ of only 1.92%. In aviation, this irregular growth method can be applied to wing rib structures with voids, preserving the aerodynamic shape during elasticity and enabling morphing wings under dynamic loads. (Fig. 6e). We also present a static cloaking design for a wing rib structure with circular voids, as depicted in Supplementary Fig. 22, in which the Δ value of the cloak structure decreases from 47.78% (in the void structure) to 4.41%, representing a 90.77% reduction. Overall, the proposed approach offers significant promise for broad and impactful applications across diverse domains.

Methods

The design of building blocks

In this work, the primary objective in determining the geometric characteristics of a unit cell is to achieve varying stiffness levels among the building blocks. To simplify the fabrication of specimens—considering potential constraints on the overall structure's dimensions and minimum feature size—we prioritize lower configuration complexity in the designed building blocks. As a result, we employ a step-by-step material removal approach — that is, gradually introducing voids to incrementally increase the porosity — thereby generating building blocks with varying stiffness. This process starts with a solid block without any void and is combined with simulation analysis to identify the optimal geometric configurations.

Stiffness calculation of building blocks

The stiffness of building blocks is calculated through uniaxial compression testing on a 3×3 lattice structure composed of individual blocks (Supplementary Fig. 23a). The constituent material has a Young's modulus E=1.2 GPa and Poisson's ratio v=0.35. In the simulation, a displacement load is applied to the upper plate, inducing a 10% strain in the structure, while the lower support plate remained fixed. A friction coefficient of 0.05 is set between the structure and the two plates. Based on the force-displacement curve (Supplementary Fig. 23b), the stiffness is calculated through the formula k=F/d, where F is the force applied, and d is the displacement. All these simulations were performed in Abaqus.

Finite Element Method (FEM) simulation

The code for the irregular growth method is written in MATLAB, while the overall structures were modeled in COMSOL Multiphysics 5.6. The FEM model utilized triangular elements with a maximum size not exceeding 0.25 mm. First, the algorithm generated the matrix parameters containing information on the relative positions, cloak regions, and specific distribution. Then, according to the matrix, the numerical model is constructed. Using the numerical results, we calculated three

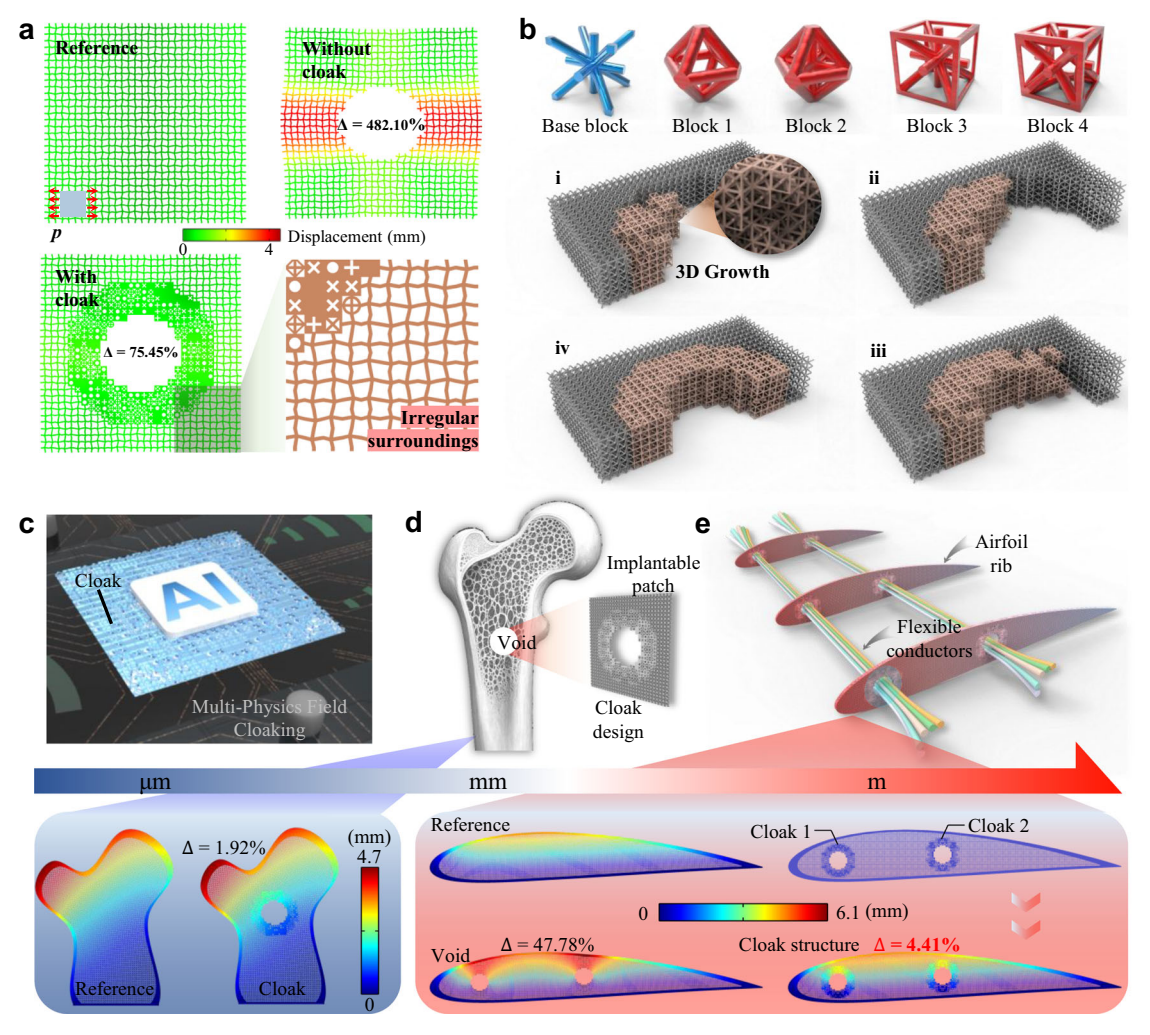


Fig. 6 | **Expansions and potential applications. a** Irregular cloaks mitigate structural distortion from voids even in aperiodic surroundings. **b** A 3D cloak structure generated by 3D irregular growth. **c** The method extends to multi-field mechanical cloaking in small-scale electronics. **d** Cloaks have the potential to

reduce damage from surgical devices on bone tissue. **e** In aviation, cloaks hold promise for preserving wing rib aerodynamics and enabling morphing wings with camouflage capabilities (Insets: Comparisons between the displacement fields of the reference and cloak structures).

principal indexes Δ_u , Δ_v and Δ . This procedure is repeated until the maximum iteration is reached.

Experimental testing of cloaking and camouflage performance

Experimental testing is performed using a Instron 3382 testing station with a load limitation of 100 kN. The experiment set up is illustrated in Supplementary Fig. S24. The upper and lower extremities of specimen were specifically designed to facilitate griping. The high-resolution camera is employed to capture the state of the specimen during specific loading phases. Digital Image Correlation (DIC) analysis is conducted using GOM Correlate software. Black spots were sprayed on the specimen surface to facilitate image tracking, enabling calculation of the displacement of each point. Due to the symmetry, a quarter of the structure is selected to calculate relative differences for simplicity.

Data availability

All data needed to evaluate the conclusions in the paper are present in the paper and/or the Supplementary Materials. The raw data can be accessed at https://doi.org/10.6084/m9.figshare.29975335.v1.

Code availability

The codes that support the findings of this study can be accessed at https://codeocean.com/capsule/6287444/tree.

References

- Saccone, M. A., Gallivan, R. A., Narita, K., Yee, D. W. & Greer, J. R. Additive manufacturing of micro-architected metals via hydrogel infusion. *Nature* 612, 685–690 (2022).
- Vangelatos, Z. et al. Strength through defects: a novel Bayesian approach for the optimization of architected materials. Sci. Adv. 7, eabk2218 (2021).
- Xia, X., Spadaccini, C. M. & Greer, J. R. Responsive materials architected in space and time. Nat. Rev. Mater. 7, 683–701 (2022).
- Bertoldi, K., Vitelli, V., Christensen, J. & van Hecke, M. Flexible mechanical metamaterials. Nat. Rev. Mater. 2. 1–11 (2017).
- Kim, J. & Torquato, S. Multifunctional composites for elastic and electromagnetic wave propagation. *Proc. Natl. Acad. Sci. USA* 117, 8764–8774 (2020).
- Kadic, M., Milton, G. W., Van Hecke, M. & Wegener, M. 3D metamaterials. *Nat. Rev. Phys.* 1, 198–210 (2019).
- Xia, Y., Gao, W. & Gao, C. A review on graphene-based electromagnetic functional materials: electromagnetic wave shielding and absorption. Adv. Funct. Mater. 32, 2204591 (2022).
- 8. García-Chocano, V. M., Christensen, J. & Sánchez-Dehesa, J. Negative refraction and energy funneling by hyperbolic materials: an experimental demonstration in acoustics. *Phys. Rev. Lett.* **112**, 144301 (2014).

- Lu, J., Deng, W., Huang, X., Ke, M. & Liu, Z. Non-Hermitian topological phononic metamaterials. Adv. Mater. 2307998 https://doi.org/10.1002/adma.202307998 (2023).
- Hu, B. et al. Non-Hermitian topological whispering gallery. *Nature* 597, 655–659 (2021).
- 11. Lipton, J. I. et al. Handedness in shearing auxetics creates rigid and compliant structures. *Science* **360**, 632–635 (2018).
- Lee, R. H., Mulder, E. A. B. & Hopkins, J. B. Mechanical neural networks: architected materials that learn behaviors. Sci. Robot. 7, eabq7278 (2022).
- 13. Zheng, X. et al. Ultralight, ultrastiff mechanical metamaterials. Science **344**, 1373–1377 (2014).
- Liu, Y. et al. Ultrastiff metamaterials generated through a multilayer strategy and topology optimization. Nat. Commun. 15, 2984 (2024).
- Schaedler, T. A. et al. Ultralight metallic microlattices. Science 334, 962–965 (2011).
- Feng, J. et al. Higher stiffness hierarchical embedded strengthening honeycomb metastructure with small negative Poisson's ratio reduction. *Thin-Walled Struct.* 179, 109561 (2022).
- Pan, Y., Zhou, Y., Gao, Q. & Sun, B. A novel 3D polygonal doublenegative mechanical metamaterial with negative stiffness and negative Poisson's ratio. Compos. Struct. 331, 117878 (2024).
- Huang, C. & Chen, L. Negative Poisson's Ratio in Modern Functional Materials. Adv. Mater. 28, 8079–8096 (2016).
- Li, Q., Yang, D., Ren, C. & Mao, X. A systematic group of multidirectional buckling-based negative stiffness metamaterials. *Int. J. Mech. Sci.* 232, 107611 (2022).
- Hewage, T. A. M., Alderson, K. L., Alderson, A. & Scarpa, F. Doublenegative mechanical metamaterials displaying simultaneous negative stiffness and negative Poisson's ratio properties. *Adv. Mater.* 28, 10323–10332 (2016).
- Wang, A., Meng, Z. & Chen, C. Q. Non-Hermitian topology in static mechanical metamaterials. Sci. Adv. 9, eadf7299 (2023).
- Meng, Z., Liu, M., Yan, H., Genin, G. M. & Chen, C. Q. Deployable mechanical metamaterials with multistep programmable transformation. Sci. Adv. 8, eabn5460 (2022).
- 23. Wang, Y., Yi, C., Tian, W., Liu, F. & Cheng, G. J. Free-space direct nanoscale 3D printing of metals and alloys enabled by two-photon decomposition and ultrafast optical trapping. *Nat. Mater.* 1–9 https://doi.org/10.1038/s41563-024-01984-z (2024).
- Zheng, X. et al. Multiscale metallic metamaterials. Nat. Mater. 15, 1100–1106 (2016).
- Del Valle Inclan Redondo, Y. et al. Non-reciprocal band structures in an exciton-polariton Floquet optical lattice. *Nat. Photon.* 18, 548-553 (2024).
- Kang, S. et al. Self-adaptive 3D lattice for curved sandwich structures. Addit. Manuf. 54, 102761 (2022).
- 27. Wu, Y. et al. Evaluation of different culture techniques of osteoblasts on 3D scaffolds. *Open Life Sci.* **5**, 456–465 (2010).
- Mutlu AviNç, G. Learning from nature for sustainable solutions in architecture: biomimetic lightweight structure designs. *Int. East. Anatol. Sci. Eng. Des. J.* 5, 198–214 (2023).
- 29. Carlquist, S. Living cells in Wood 3. overview; functional anatomy of the parenchyma network. *Bot. Rev.* **84**, 242–294 (2018).
- 30. Pham, M.-S., Liu, C., Todd, I. & Lertthanasarn, J. Damage-tolerant architected materials inspired by crystal microstructure. *Nature* **565**, 305–311 (2019).
- Bhuwal, A. S., Pang, Y., Ashcroft, I., Sun, W. & Liu, T. Discovery of quasi-disordered truss metamaterials inspired by natural cellular materials. J. Mech. Phys. Solids 175, 105294 (2023).
- 32. Liu, C., Lertthanasarn, J. & Pham, M.-S. The origin of the boundary strengthening in polycrystal-inspired architected materials. *Nat. Commun.* **12**, 4600 (2021).
- 33. Imediegwu, C. et al. Mechanical characterisation of novel aperiodic lattice structures. *Mater. Des.* **229**, 111922 (2023).

- 34. Liu, K., Sun, R. & Daraio, C. Growth rules for irregular architected materials with programmable properties. *Science* **377**, 975–981 (2022)
- 35. Heyde, A., Guo, L., Jost, C., Theraulaz, G. & Mahadevan, L. Selforganized biotectonics of termite nests. *Proc. Natl. Acad. Sci. USA* **118**, e2006985118 (2021).
- 36. Bonfanti, S., Guerra, R., Font-Clos, F., Rayneau-Kirkhope, D. & Zapperi, S. Automatic design of mechanical metamaterial actuators. *Nat. Commun.* **11**, 4162 (2020).
- Goodrich, C. P., Liu, A. J. & Nagel, S. R. The principle of independent bond-level response: tuning by pruning to exploit disorder for global behavior. *Phys. Rev. Lett.* 114, 225501 (2015).
- 38. Luan, S., Chen, E., John, J. & Gaitanaros, S. A data-driven framework for structure-property correlation in ordered and disordered cellular metamaterials. Sci. Adv. 9, eadi1453 (2023).
- Jia, Y., Liu, K. & Zhang, X. S. Modulate stress distribution with bioinspired irregular architected materials towards optimal tissue support. *Nat. Commun.* 15, 4072 (2024).
- Liu, Y., Xia, B., Liu, K., Zhou, Y. & Wei, K. Robustness and diversity of disordered structures on sound absorption and deformation resistance. J. Mech. Phys. Solids 190, 105751 (2024).
- 41. Wang, X. et al. Unprecedented strength enhancement observed in interpenetrating phase composites of aperiodic lattice metamaterials. *Adv. Funct. Mater.* **35**, 2406890 (2024).
- 42. Hu, X. et al. Multiband omnidirectional invisibility cloak. *Adv. Sci.* **11**, 2401295 (2024).
- Schurig, D. et al. Metamaterial electromagnetic cloak at microwave frequencies. Science 314, 977–980 (2006).
- 44. Zhang, B. & Wu, B.-I. Electromagnetic detection of a perfect invisibility cloak. *Phys. Rev. Lett.* **103**, 243901 (2009).
- 45. Valentine, J., Li, J., Zentgraf, T., Bartal, G. & Zhang, X. An optical cloak made of dielectrics. *Nat. Mater.* **8**, 568–571 (2009).
- 46. Slovick, B. & Hellhake, J. Inverse design of invisibility cloaks using the optical theorem. *Photon. Res.* **10**, 974 (2022).
- Li, Y. et al. Temperature-dependent transformation thermotics: from switchable thermal cloaks to macroscopic thermal diodes. *Phys. Rev. Lett.* 115, 195503 (2015).
- Wang, Y., Sha, W., Xiao, M., Qiu, C. & Gao, L. Deep-learning-enabled intelligent design of thermal metamaterials. *Adv. Mater.* 35, 2302387 (2023).
- García-Chocano, V. M. et al. Acoustic cloak for airborne sound by inverse design. Appl. Phys. Lett. 99, 074102 (2011).
- Lian, M. et al. Acoustic transmissive cloaking with adjustable capacity to the incident direction. *Microsyst. Nanoeng.* 8, 108 (2022).
- Milton, G. W., Briane, M. & Willis, J. R. On cloaking for elasticity and physical equations with a transformation invariant form. N. J. Phys. 8, 248–248 (2006).
- 52. Bückmann, T., Kadic, M., Schittny, R. & Wegener, M. Mechanical cloak design by direct lattice transformation. *Proc. Natl. Acad. Sci. USA* **112**, 4930–4934 (2015).
- 53. Wang, L. et al. Mechanical cloak via data-driven aperiodic metamaterial design. *Proc. Natl. Acad. Sci. USA* **119**, e2122185119 (2022).
- 54. Kadic, M. et al. Elastodynamic behavior of mechanical cloaks designed by direct lattice transformations. *Wave Motion* **92**, 102419 (2020).
- 55. Hai, L., Zhao, Q. & Meng, Y. Unfeelable mechanical cloak based on proportional parameter transform in bimode structures. *Adv. Funct. Mater.* **28**, 1801473 (2018).
- Bückmann, T., Thiel, M., Kadic, M., Schittny, R. & Wegener, M. An elasto-mechanical unfeelability cloak made of pentamode metamaterials. *Nat. Commun.* 5, 4130 (2014).
- Lu, Y. & Tong, L. Concurrent multiscale topology optimization of metamaterials for mechanical cloak. *Comput. Methods Appl. Mech. Eng.* 409, 115966 (2023).

- Cheng, X. et al. A compatible boundary condition-based topology optimization paradigm for static mechanical cloak design. *Extrem. Mech. Lett.* 65, 102100 (2023).
- Balci, O., Polat, E. O., Kakenov, N. & Kocabas, C. Graphene-enabled electrically switchable radar-absorbing surfaces. *Nat. Commun.* 6, 6628 (2015).
- 60. Zhu, H. et al. High-temperature infrared camouflage with efficient thermal management. *Light Sci. Appl.* **9**, 60 (2020).
- Zhu, H. et al. Multispectral camouflage for infrared, visible, lasers and microwave with radiative cooling. *Nat. Commun.* 12, 1805 (2021).
- Wang, X., Meng, Z. & Chen, C. Q. Enhancing haptic continuity in virtual reality using a continuity reinforcement skeleton. *Nat. Commun.* 16, 2995 (2025).
- Khairallah, S. A. et al. Controlling interdependent mesonanosecond dynamics and defect generation in metal 3D printing. Science 368, 660–665 (2020).
- Basak, A., Acharya, R. & Das, S. Epitaxial deposition of nickel-based superalloy René 142 through scanning laser epitaxy (SLE). Addit. Manuf. 22, 665–671 (2018).

Acknowledgements

This work is supported by the National Natural Science Foundation of China (NSFC) under Grant Nos. 12272298, 12572105 to B. L., 12202232 to J. Y. and 12232001 to Z. L. This work is also supported by the Fundamental Research Funds for the Central Universities under Grant No. D5000250252 to B. L.

Author contributions

Z.Y. and J.L.Y. contributed equally to this work. Conceptualization: Z.Y., B.L., F.L.L., J.L.Y., and J.C. Funding acquisition: B.L., J.L.Y., and Z.L. Methodology: Z.Y. and J.L.Y. Investigation: Z.Y., J.L.Y., F.L.L., L.Y., B.L., and J.C. Validation: Z.Y., J.L.Y., F.L.L., Z.L., L.Y., and B.L. Visualization: Z.Y., J.L.Y., F.L.L., B.L., and J.C. Supervision: B.L., J.C., Z.L., and L.Y. Writing-original draft: Z.Y. and J.L.Y. Writing-review and editing: B.L., J.C., Z.L., and L.Y. All authors contributed to scientific discussions and modifications of the manuscript.

Competing interests

The authors declare no competing interests.

Additional information

Supplementary information The online version contains supplementary material available at https://doi.org/10.1038/s41467-025-63939-5.

Correspondence and requests for materials should be addressed to Bing Li or Johan Christensen.

Peer review information *Nature Communications* thanks the anonymous reviewers for their contribution to the peer review of this work. A peer review file is available.

Reprints and permissions information is available at http://www.nature.com/reprints

Publisher's note Springer Nature remains neutral with regard to jurisdictional claims in published maps and institutional affiliations.

Open Access This article is licensed under a Creative Commons Attribution-NonCommercial-NoDerivatives 4.0 International License, which permits any non-commercial use, sharing, distribution and reproduction in any medium or format, as long as you give appropriate credit to the original author(s) and the source, provide a link to the Creative Commons licence, and indicate if you modified the licensed material. You do not have permission under this licence to share adapted material derived from this article or parts of it. The images or other third party material in this article are included in the article's Creative Commons licence, unless indicated otherwise in a credit line to the material. If material is not included in the article's Creative Commons licence and your intended use is not permitted by statutory regulation or exceeds the permitted use, you will need to obtain permission directly from the copyright holder. To view a copy of this licence, visit http://creativecommons.org/licenses/by-nc-nd/4.0/.

© The Author(s) 2025